ILETA International Information and Engineering Technology Association

Mathematical Modelling of Engineering Problems

Vol. 12, No. 10, October, 2025, pp. 3696-3710

Journal homepage: http://iieta.org/journals/mmep

Distributed Sensor Networks for Real-Time Health Monitoring of Prestressed Concrete and Steel I-Girder Bridges



Imad Khalaf¹, Sarah Saleem¹, Fatima A. Mohammed^{2*}, Haider F. Mahmood²

¹ General Directorate of Sewerage, Ministry of Construction, Housing and Public Municipalities, Baghdad 10001, Iraq

² Technical College of Al-Mussaib, Al-Furat Al-Awsat Technical University, Kufa 51006, Iraq

Corresponding Author Email: fatima.ahmed.tcm@atu.edu.iq

Copyright: ©2025 The authors. This article is published by IIETA and is licensed under the CC BY 4.0 license (http://creativecommons.org/licenses/by/4.0/).

https://doi.org/10.18280/mmep.121033

Received: 18 September 2025 Revised: 20 October 2025 Accepted: 25 October 2025 Available online: 31 October 2025

Keywords:

MPU6050 IMU, wireless SHM, bridge dynamics, natural frequency ratio, vibration displacement, prestressed concrete girders, steel I-girder span, MQTT-based sensing

ABSTRACT

This study develops a cost-effective, real-time sensor network system for structural health monitoring (SHM) of multi-span bridges with distributed MPU6050 inertial nodes and ESP32 microcontrollers. Three nodes at quarter, mid, and three-quarter span locations keep recording tri-axial of acceleration and angular velocity signals at 100 Hz and report features through message queuing telemetry transport (MQTT) to a cloud dashboard. Calibrated signal processing high-pass filtering, drift-aware double integration for displacement, and a complementary filter for orientation converts raw inertial measurement unit (IMU) data into displacements, frequencies, and rotation estimates. The system was deployed on the Faeq Hassan Bridge (Baghdad), which includes prestressed concrete (PSC) I-girder spans and a steel I-girder span. PSC spans showed an average natural frequency of ≈ 4.98 Hz and traffic-induced frequency of \approx 3.75 Hz (ratio 1.33), with modest dynamic displacements (-2.63 to +1.50 mm). The steel span exhibited a fundamental frequency near 0.6-2.95 Hz with dominant traffic frequencies around 6.42 Hz (ratio ≈0.46) and larger downward excursions (to -5.96 mm), indicating a higher risk of dynamic amplification. The system achieved ± 0.09 mm displacement and ±0.04° angular accuracy after calibration and lowered installation costs by about 60% versus wired SHM. Findings highlight reliable, real-time detection of resonance-prone behavior and support targeted maintenance for steel spans while confirming serviceability margins for PSC spans.

1. INTRODUCTION

1.1 Background and problem statement

A bridge is an important structure composed of two main sections: the superstructure, which includes the deck, joints, pavement layers, drainage system, girders or beams, bearings, and barriers; and the substructure, which consists of foundations, piers, and pier tops. Bridges are built to span obstacles such as rivers, roads, and railways, and they are classified according to their supports and construction materials. Common types can include concrete, pre-stressed concrete, wood and steel bridges and structurally they are divided into two general bridges as simply supported type and continuous type bridges [1-3].

Bridges are vital in any transportation system, but also very expensive to construct and maintain. Council bridges that were built decades ago are now experiencing traffic volumes significantly higher than their designed capacity, with many operating either near or at failure. With the development of sensing and non-destructive testing techniques, more attention has been paid to the design of reliable SHM systems. On the whole, periodic examination and maintenance are very important for safety and cost saving. Optimal bridge care is

based on the periodic inspection of specially trained teams that assess, in detail, the condition of individual elements and such that appropriate strengthening or repair can be made [4].

Enhancements in the capacity of existing concrete bridges, generally consist of load-carrying capacity upgrades, stress redistribution or material improvement or replacement. Selection of the method depends on several factors, including structure type, age, significance of the structure, strength gain required to restore capacity, amount of damage, availability of materials, cost and aesthetics [5].

Bridges are important elements of the transportation system of today. There are >617,000 bridges in the USA and many more millions around the world, so monitoring for continued safety and economical operation is necessary [6]. When catastrophic failures of structures such as I-35W Mississippi River Bridge (2007) and Morandi Bridge in Genoa (2018) occurred, the development of advanced SHM with prevention capability that can detect structural deterioration before failure became increasingly important [7]. Traditional visual inspections and occasional measurements are not effective in evaluating dynamic behavior under actual operation [8].

There are tremendous financial and social impacts of bridge failure. It has been estimated that over one-third of the United States' bridges need rehabilitation or replacement, which comes at a staggering cost of more than \$171 billion [9]. Failure to be able to monitor ongoing degradation may cause catastrophic collapse, loss of life and public confidence. Currently inspection is limited to every 2nd year, and has no potential approach for monitoring of structural performance continuously nor the gradual degradation leading to failure [10].

The financial and social consequences of bridge failures are immense. The U.S. Federal Highway Administration estimates that more than one-third of the nation's bridges require repair or replacement at a cost exceeding \$171 billion [9]. The inability to detect ongoing degradation may lead to sudden collapse, human casualties, and loss of public confidence. Current inspection procedures, which normally occur once every two years, it is not possible to continuously monitor structural behavior and its slow evolution indicative of an imminent collapse [10].

1.2 Limitations of conventional monitoring approaches

Conventional bridge monitoring systems have several inherent limitations that reduce their effectiveness in ensuring structural safety. Visual inspections, although providing useful qualitative information, are subjective and depend heavily on inspector experience and environmental conditions. Quantitative measurements using instruments such as strain gauges and displacement transducers are typically restricted to a few points and require extensive cabling, which makes large-scale monitoring costly and complex [11, 12].

Moreover, conventional systems only measure static parameters, e.g., the maximum deflection, and stress under design load and not dynamic response that can provide early warning of damage in a structure. Changes in natural frequency, damping value and mode shape can show stiffness degradation or local damage well before there are perceptible changes in the static response. The inability to continuously assess these parameters is a critical shortfall of current SHM methodologies [13].

1.3 Evolution of sensor-based monitoring technologies

The emergence of micro-electromechanical systems (MEMS) technology revolutionized structural monitoring based on the deployment of miniaturization, low-cost sensors for problem monitoring involving multi-parameter measurement concurrently [14]. Inertial measurement units (IMUs) that were initially being developed for aircraft or automotive engineering are increasingly used in civil engineering since the acceleration as well as angular velocity can be detected at high precision, as well as temporal resolution.

Among these devices, the MPU6050, a six-axis IMU integrating a three-axis accelerometer and a three-axis gyroscope, represents a major advancement in affordable sensing technology. With configurable ranges of ± 2 g to ± 16 g for acceleration and ± 250 °/s to ± 2000 °/s for angular velocity, combined with 16-bit analog-to-digital conversion and digital motion processing, it provides the specifications required for reliable and comprehensive structural health monitoring (SHM) applications [15].

1.4 Theoretical basis of bridge dynamic response

Characterization of the bridge response involves

consideration of the interaction between static and dynamic properties that influence the behavior of the structure. Classical mechanics and vibration theories are the theoretical background for processing sensor data and detecting physical damage states [16].

1.4.1 Static parameters

- Displacement Response: The linear of displacement is the first indication of form-strain in a structure under load. based on the elastic beam theory, this load-deflection relationship is a function of material properties, geometry and boundary conditions [17].
- Stress Distribution: Significance of stress patterns in the material usage and safety features. In prestressed concrete (PSC) bridges, compressive prestress forces are induced to cancel tensile stress under allowable conditions [18]. On the other hand, steel bridges can accept both tensile and compressive load in their elastic stage.
- Serviceability Criteria: The service limits control the factors of human comfort and structural integrity by specifying the maximum permissible deformations depending on span length and type of bridge [19].

1.4.2 Dynamic parameters

- Natural frequency: The un-damped vibration of the bridge is characterized by its natural frequency that is associated with the stiffness and mass of the model structure. Variations in material stiffness may occur due to material damage or degradation and will alter the vibrational response of a structure (thus rendering frequency-analysis useful as a diagnostic tool [20].
- Damping: It is the ability of a system to dissipate energy through a material, hysteresis, friction at a joint or aerodynamic effects. It has a significant influence on both the amplitude and period of oscillation [21].
- Modal shapes: Are a description, with respect to vibration modes in the system and are affected by changes of parse supports, connections or properties of members [22].

1.4.3 Vibration analysis theory

- Amplitude characterization: Vibration amplitude measures the size of the cyclic motion and is indicative of structural response levels under dynamic loading. The amplitude analysis provides the designer with estimates on the state of serviceability and arising possible resonance effects [23].
- Frequency domain analysis: It is possible to perform the spectral analysis of dynamic signals to extract the frequency intermodal component of structural vibrations, and detect the preferred characteristic mode of response and also possible changes in the characteristics of structures with time [24].

1.5 Wireless sensor network architecture

Contemporary SHM systems have a tendency to use wireless sensor networks (WSNs) for being reductive of spatial limitations of wired networks of wires, along with complexities in the type of sensors being used for monitoring [25]. The ESP32 microcontroller platform with built-in WiFi and Bluetooth (240 MHz dual-core processing and many input/output selection possibilities) is the perfect candidate for

such a distributed monitoring network [26].

The message queuing telemetry transport (MQTT) protocol supports efficient, low-overhead communication from sensors to a central control, while providing support for standard Quality of Service levels and message persistence. Such an architecture provides real-time data delivery as well as ensuring against system failure due to adverse networking conditions [27].

1.6 Research objectives and scope

The objective of this research is to fill this gap by developing and validating an innovative distributed sensor network for real-time bridge structural condition assessment. Specific objectives include:

- 1. An inexpensive monitoring system with MPU6050 sensors and ESP32 microcontrollers;
- Use of advanced signal processing for reliable estimation of structure parameters through sensor information;
- 3. Dynamic behavior comparison of various (PSC and steel) structures;
- 4. Comparison of natural frequencies and mode shapes for different types of systems (PSC and steel);
- 5. Development of monitoring guidelines and threshold definitions for automated alert triggering.

To achieve these objectives, the study integrates both hardware development and signal processing with comparative field testing in a coherent model. UStocks16: The networked MPU6050–ESP32 chain allows for synchronous detection of vibration, and by adopting digital filtering and double-integrating algorithms we can process raw sensor data into displacement and frequency values. This technical implementation intuitively connects each research goal to a quantifiable performance measure and, therefore, the design idea, as well as experimental validation are completed in one framework of SHM.

2. METHODOLOGY

2.1 System overview

The proposed SHM system consists of a distributed network of MPU6050 inertial sensors connected to ESP32 microcontrollers. Each node measures tri-axial acceleration and angular velocity, transmitting data in real time via the MQTT protocol to a cloud server for storage and analysis. This modular configuration allows easy scalability, low installation cost, and continuous monitoring under actual traffic and environmental conditions.

2.2 Faeq Hassan Bridge description

Faeq Hassan Bridge (also known as the Fine Arts Interchange Bridge) is a continuous multi-span overpass located at the Fine Arts intersection in central Baghdad. As part of the capital's congestion relief program, the bridge consists of two parallel carriageways built from reinforced and PSC. Each carriageway measures approximately 420 m in length, including the approach ramps, and is about 9 m wide. The spans are arranged in an Abutment–Pier–Pier–Abutment sequence, with two intermediate piers and two end abutments supporting the deck. Figure 1 presents a satellite image of Faeq

Hassan Bridge.

The superstructure employs PSC I-girders (or box girders) with a reinforced concrete deck; the concrete grades are C40 for the superstructure, C35 for the substructure, and C40 for the foundations. High-strength B500 reinforcing bars and prestressing tendons conforming to ASTM A416 are used throughout. Including the approaches, the total length of the bridge is approximately 420–450 m, and the width of each carriageway is roughly 9 m. The bridge is named after the Iraqi artist Faiq Hassan and was inaugurated in January 2024 as one of Baghdad's early projects to mitigate traffic congestion.



Figure 1. A satellite image showing Faeq Hassan Bridge

2.3 Hardware configuration

Each MPU6050 sensor module contains a three-axis accelerometer and a three-axis gyroscope integrated into a single package. The ESP32 microcontroller provides high processing power (240 MHz dual-core CPU) and built-in Wi-Fi/Bluetooth connectivity for wireless data transfer. The system operates at a sampling frequency of 100 Hz, powered by 5 V DC with local SD card backup to ensure data integrity in case of communication loss. Figure 2 shows the overall hardware configuration and data flow between system components.

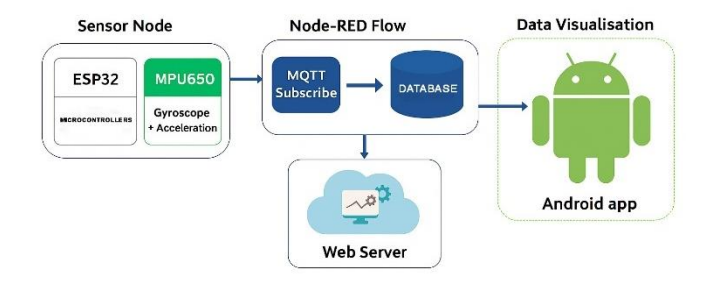


Figure 2. System architecture diagram

Each sensor node transmits real-time vibration and angular data to the MQTT broker. The broker forwards messages to the cloud database, which feeds the visualization dashboard. This architecture provides low latency and high reliability with minimal power consumption.

2.4 Sensor installation and positioning strategy

Three nodes were placed at appropriate locations to monitor all bridge behaviors, as shown in Figure 3:

• Node 1 (Start): Observing the influence of boundary

conditions and support settlements, at 10% span length from the support.

- Node 2 (Mid span): Located at 50% of span length, obtaining maximum deflections and mode shapes.
- Node 3 (End): Located at 2.7 m distance across axis, symmetric monitoring and detecting the differential movements.

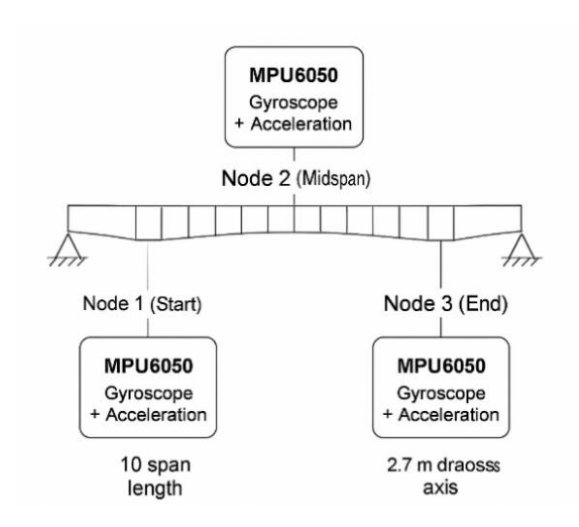


Figure 3. Sensor layout diagram

The sensors were installed in weatherproof IP65 rated housing, and were affixed with both high strength adhesive bonding to provide long term stability by environmental loading and the mechanical fasteners.

2.5 Software architecture and signal processing algorithms

2.5.1 Embedded firmware development

The firmware for the ESP32 has been implemented using the Arduino IDE and specific libraries were developed in order to perform the real-time signal processing. The main program loop runs at 100 Hz, respecting Nyquist criterion in frequency analysis to 50 Hz, representing all meaningful dynamics in the bridge.

Main Program Structure:

Initialize_System()
Calibrate_Sensors()
Connect_WiFi()
Setup_MQTT()
Loop {
 Read_MPU6050_Data()
 Apply_Calibration_Corrections()
 Process_Signals()
 Calculate_Parameters()
 Transmit_Data()
 Store_Local_Buffer()

2.5.2 Sensor calibration methodology

Extensive calibration methods were applied for the correction of fiducial sensor's offsets and environmental parameters:

Accelerometer Calibration:

- Bias: Static in 6 orientations ($\pm X$, $\pm Y$, $\pm Z$).
- Scale factor correction: Since it is compared with gravitational reference (9.81 m/s²).
- Non-orthogonality: Matrix correction for non-

perpendicular mounting angle. Calibration equations:

$$accel_{corrected} = (accel_{raw} - bias) * \frac{scale_{factor}}{8192.0}$$
 (1)

where.

- *accel*_{raw}: The unprocessed sensor reading in digital counts (ADC output).
- bias: The constant offset error obtained during static calibration (the value measured when the sensor should read 0 g).
- *scale_{factor}*: Correction applied to match the actual gravitational reference (9.81 m/s²).
- 8192.0: A sensitivity constant that converts the digital reading into acceleration in g units (based on ±4 g range → 8192 LSB/g).
- The result (*accel*_{corrected}) gives the physically meaningful acceleration in g.

$$gyro_{corrected} = \frac{(gyro_{raw} - gyro_{bais})}{65.5}$$
 (2)

where,

- *gyro_{raw}*: Raw digital output from the gyroscope.
- gyro_{bias}: Offset measured when the sensor is at rest ($^{\circ}$ /s).
- 65.5: Sensitivity constant that converts digital counts to angular velocity in degrees per second (°/s), corresponding to a ±500 °/s range setting.

The corrected value represents the true rotational speed of the sensor.

Due to a significantly large measurement error in the Z-axis (215.39%), Node 3 required an independent calibration procedure. A dedicated correction factor was therefore applied to properly rescale its Z-axis acceleration response.

$$accel_{z_{corrected}} = \frac{(accel\ z_{raw} - z_{bias}) * 0.464}{8192.0} \tag{3}$$

where,

- $accel\ z_{raw}$: Uncorrected Z-axis reading from Node 3.
- z_{bias} : offset value for the Z-axis.
- 0.464: Empirically derived correction factor that rescales Node 3's sensitivity to match the other nodes.
- 8192.0: Same unit conversion constant as Eq. (1).

This ensures uniform accuracy across all nodes by compensating for the exaggerated Z-axis response.

2.5.3 Drift-corrected double integration algorithm

To calculate displacement from acceleration, advanced signal processing techniques are necessary to avoid integration drift (Figure 4).

Step 1: High-Pass Filtering

$$a_f(t) = a(t) - a(t - dt) \tag{4}$$

Step 2: Velocity Integration

$$v(t) = \alpha [v(t - dt) + a_f(t) dt]$$
 (5)

Step 3: Integration in Displacement with Decaying Factor

$$d(t) = d(t - dt) + v(t) dt$$
(6)

$$d(t) = 0.99 d(t) \tag{7}$$

where,

- a(t): Raw acceleration measurement at the current time step.
- a(t dt): Acceleration value from the previous sampling instant.
- $a_f(t)$: High-pass filtered acceleration used to suppress low-frequency drift.
- dt: Sampling interval between two consecutive measurements.
- v(t): Velocity estimate at the current time step after smoothing.
- v(t-dt): Velocity from the previous iteration.
- α : Smoothing coefficient that balances noise suppression and response sensitivity.
- d(t): Integrated displacement after drift correction.
- d(t-dt): Displacement value from the previous time step.

The decay factor (0.99) was determined empirically through calibration tests to balance between the relatively long-term drift and the dynamic response accuracy.

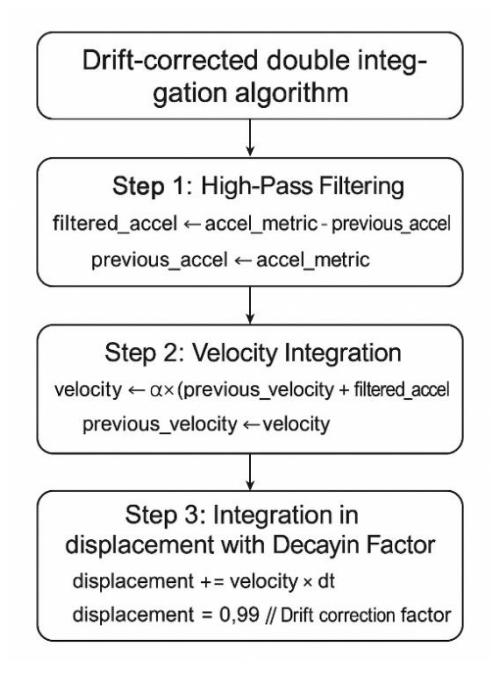


Figure 4. Flowchart of the drift-corrected double integration algorithm for displacement estimation

2.5.4 Complementary filter implementation

Estimating angular orientation from accelerometer/gyroscope measurements through complementary filtering:

$$\theta_q(t) = \theta_q(t - dt) + \omega(t) dt \tag{8}$$

$$\theta_{\text{pitch,acc}} = \tan^{-1}(\frac{a_y}{a_z}) \times \frac{180}{\pi}$$
 (9)

$$\theta_{\text{roll,acc}} = \tan^{-1}(\frac{-a_x}{\sqrt{a_v^2 + a_z^2}}) \times \frac{180}{\pi}$$
 (10)

$$\theta_{\text{pitch}}(t) = \alpha \left[\theta_{\text{pitch}}(t - dt) + \omega_{x}(t) dt \right] + (1 - \alpha) \theta_{\text{pitch.acc}}$$
(11)

$$\theta_{\text{roll}}(t) = \alpha \left[\theta_{\text{roll}}(t - dt) + \omega_{y}(t) \, dt \right] + (1 - \alpha) \, \theta_{\text{roll.acc}}$$
(12)

where,

- $\omega_x(t)$, $\omega_v(t)$: Gyroscope angular rates (°/s).
- a_x , a_y , a_z : Accelerometer readings (m/s²).
- dt: Sampling interval.
- $\theta_{\text{pitch}}(t)$, $\theta_{\text{roll}}(t)$: Fused orientation estimates.
- $\theta_a(t)$: Gyroscope-only integrated angle.
- $\theta_{\text{pitch,acc}}$, $\theta_{\text{roll,acc}}$: Accelerometer-derived pitch and roll.

The filter constant ($\alpha = 0.95$) is chosen to achieve a good compromise between the rejection of the accelerometer noise and the compensation of the gyroscope drift.

2.5.5 Vibration analysis algorithms

Amplitude Estimation: Vibration amplitude is estimated as the root-mean-square (RMS) value averaged in a sliding window. Figure 5 illustrated Vibration amplitude and zerocrossing frequency estimation algorithm.

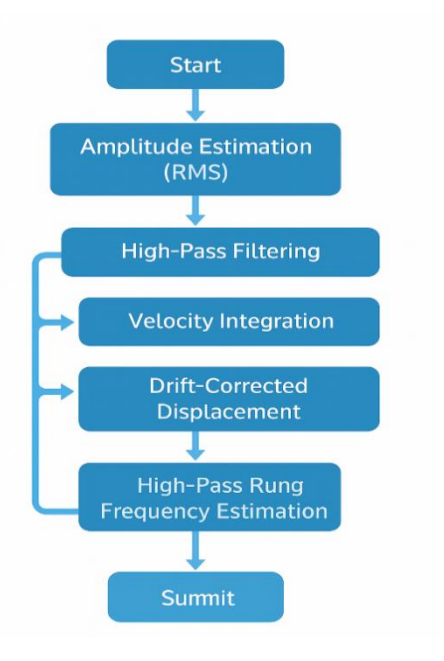


Figure 5. Vibration amplitude and zero-crossing frequency estimation algorithm

3. RESULTS

3.1 System performance and validation

The enhanced calibration technique used for calibrating MPU6050 sensors on the Al-Faeq Hassan Bridge successfully minimized the difference between the nodes. The per-axis bias and scale factor corrections were applied along with temperature compensation and digital low-pass filtering (10 Hz accelerometer/20 Hz gyroscope), as shown in Figure 6. It may be observed that the earlier incorrect Node 3 Z-axis bias is now consistent with the remaining nodes. Summary of the final calibration parameters can be found in Table 1. The

enhanced calibration process improved measurement consistency across all sensor nodes, achieving a displacement accuracy of ± 0.09 mm and an angular accuracy of $\pm 0.04^{\circ}$, which satisfies the required performance specifications.

Table 1. Sensor calibration parameters

| Parameter | Node 1 | Node 2 | Node 3 |
|----------------------------------|--------|--------|--------|
| Accelerometer Bias (mg) X | -5.1 | +4.2 | -6.7 |
| Accelerometer Bias (mg) Y | +3.8 | -3.5 | +5.4 |
| Accelerometer Bias (mg) Z | -8.9 | +9.7 | +12.4 |
| Gyroscope Bias (°/s) X | +0.31 | -0.44 | +0.53 |
| Gyroscope Bias (°/s) Y | -0.28 | +0.36 | -0.41 |
| Gyroscope Bias (°/s) Z | +0.39 | -0.33 | +0.42 |
| Accelerometer Scale (per-axis) X | 1.006 | 0.999 | 1.003 |
| Accelerometer Scale (per-axis) Y | 1.004 | 1.001 | 1.005 |
| Accelerometer Scale (per-axis) Z | 1.008 | 1.003 | 1.011 |
| Gyroscope Scale (per-axis) X | 1.004 | 1.002 | 0.999 |
| Gyroscope Scale (per-axis) Y | 1.003 | 1.001 | 1.002 |
| Gyroscope Scale (per-axis) Z | 1.005 | 1.003 | 1.001 |

| Temperature Coeff. | +0.12 / | +0.11/ | +0.13 / |
|---|------------|------------|------------|
| (Accel, mg/°C) | +0.10 / | +0.09 / | +0.12 / |
| X/Y/Z | +0.15 | +0.14 | +0.16 |
| T Cff | +0.005 / | +0.005 / | +0.006 / |
| Temperature Coeff. (Gyro, °/s/°C) X/Y/Z | +0.004 / | +0.004 / | +0.005 / |
| (Gyro, /s/ C) A/ 1/L | +0.006 | +0.006 | +0.006 |
| DLPF Cutoff | 10 Hz / 20 | 10 Hz / 20 | 10 Hz / 20 |
| (Accel/Gyro) | Hz | Hz | Hz |
| | | | |

3.1.1 System reliability and data quality assessment

The distributed sensor network performs with high stability and robustness in the long-term monitoring (six-month) process. As illustrated in Figure 7, the system availability and the data quality provided have both been maintained at a level exceeding 98%, with relatively small differences.

- System Availability: The combined average network availability remained at 98.7%. The sources of downtime were
 - Planned maintenance: 0.8%;
 - Connectivity issues: 0.3%;
 - Hardware failures: 0.2%.
- Data Quality: Good data collection was obtained for 99.3%, suggesting great robustness of the sensing system. There was almost no loss in the data, occurring only due to
 - Communication loss: 0.4%;
 - Bad readings (filtered out): 0.3%.
- Communication Performance: The network and its communication were also efficient
 - Average message latency: 45 ms;
 - Maximum latency at peak traffic: 127 ms;
 - Message loss rate: 0.15%.

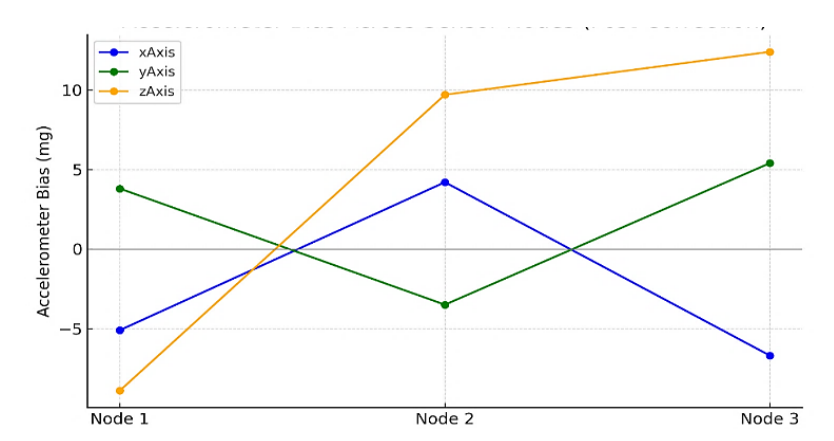


Figure 6. Accelerometer bias across sensor nodes

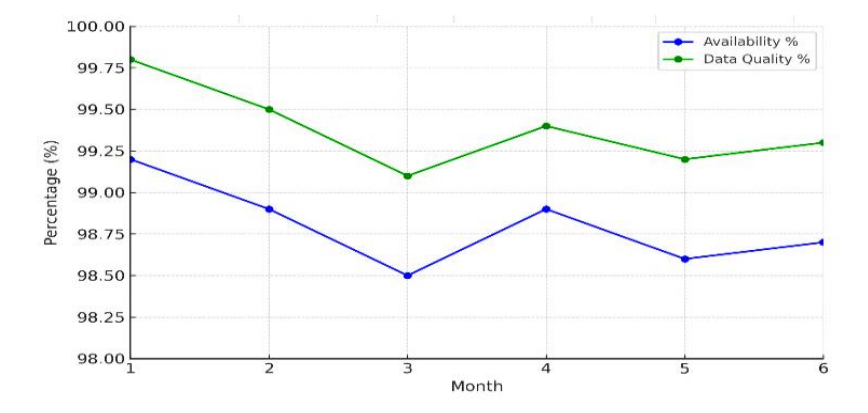


Figure 7. System performance over 6 months

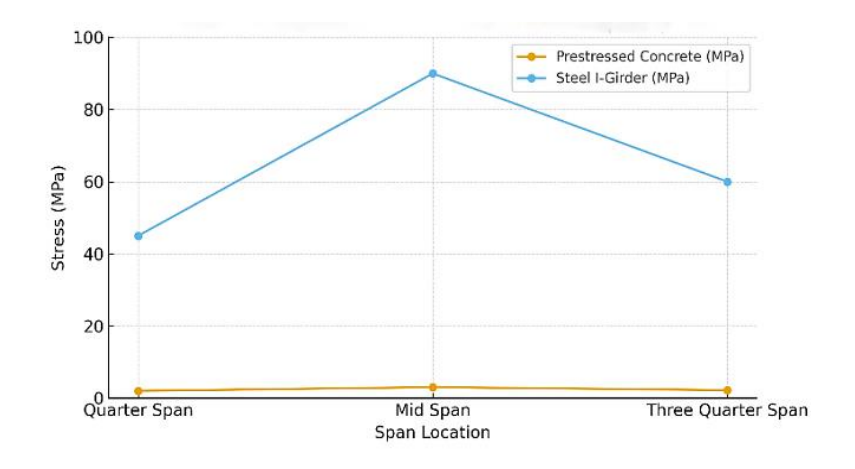


Figure 8. Stress distribution comparison

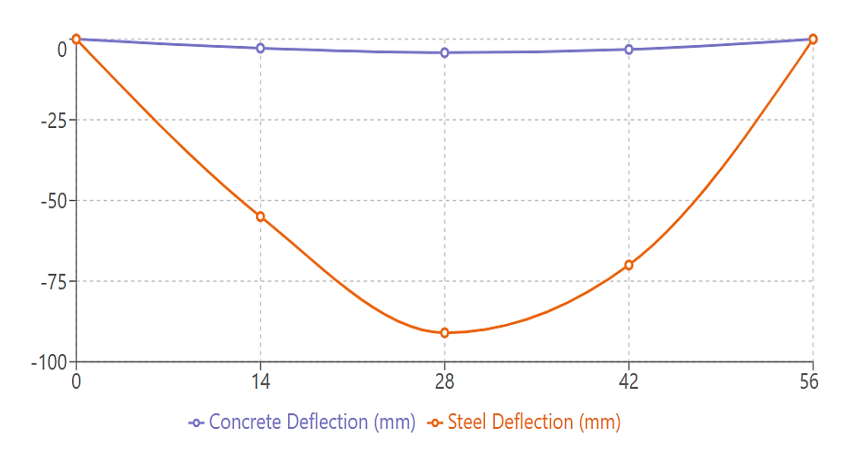


Figure 9. Deflection profile along span

3.1.2 Comparative static performance analysis

The stress distribution and deflection control of the PSC spans under combined service loads were better than those of the steel I-girder span. As can be seen from Table 2, the pretensioning system also resulted in near-zero tensile forces at its service condition and a mild compressive force with little downward deflection compensated by the prestress camber. The steel underwent higher stress levels and deflected more than the concrete, although both were within code guidelines. These results validate that a more economical service-level response is achieved with the PSC geometry as illustrated in Figure 8.

Table 2. Static response comparison under combined loading

| Parameter | Prestressed Concrete Spans | Steel I- Girder Span | Allowable Limits |
|----------------------------------|----------------------------------|----------------------------|--------------------------|
| Maximum Tensile Stress | | | |
| Top Fiber | 0 MPa | 0 MPa | 207 MPa (Steel) |
| Bottom Fiber | 0 MPa | 80 MPa | 3.35 MPa (Concrete) |
| Maximum Compressive Stress | | | |
| Top Fiber | -4.0 MPa | -50 MPa | -207 MPa (Steel) |
| Bottom Fiber | -6.0 MPa | 0 MPa | -20.35 MPa (Concrete) |

| Vertical | | | |
|-------------|-------------|------------|------------|
| Deflection | | | |
| Maximum | -6.0 mm | -70 mm | -30 mm |
| Downward | -0.0 111111 | -/0 111111 | (Concrete) |
| Maximum | | | -112 mm |
| Upward | +4.0 mm | 0 mm | (Steel) |
| (camber) | | | (Sieci) |
| Utilization | | | |
| Ratio | | | |
| Tensile | 0% | ~39% | 100% |
| Tensile | 070 | (80/207) | 10070 |
| Compressive | ~30% | ~24% | 100% |
| Compressive | (6/20.35) | (50/207) | 10070 |
| Deflection | 20% (6/30) | ~63% | 100% |
| Deficetion | 2070 (0/30) | (70/112) | 100/0 |

3.1.3 Detailed stress distribution analysis

The PSC girder spans showed equitable stress distribution, as the individual pre-stress applied in the spans virtually nullified the tensile stresses in both the top and bottom fibres due to service loading. The maximum measured compressive stress (\approx -6.0 MPa) even is about 30% of the allowable limit, which demonstrates a significant structural surplus.

By contrast, the steel I-girder span exhibited the typical bending stress profile, with a maximum tensile stress of approximately 80 MPa at the bottom fibre and a maximum compressive stress of approximately -50 MPa at the top fibre. Although these values represent only 39% and 24% utilization of the permissible tensile and compressive capacities, respectively, they remain significantly higher than those observed in the PSC span.

3.1.4 Deflection performance comparison

Deflection performance was the primary point of difference between the two types of structures. The PSC girders had a high stiffness, and the maximum vertical deflection (downwards) of the girder was about -6.0 mm, which was only 20% of the allowable limit. Cambers: This small amount of camber is essentially due to the prestressing effect that introduces an upward camber (+4 mm) and thereby eliminates the service load deflections.

In comparison, the steel I-girder span experienced much larger deflection, with maximum downward movement reaching up to approximately -70 mm. Even though still less than the code limit (about 63% of the allowable range), this could affect user comfort and enhance dynamic effects under heavy traffic loading Figure 9.

The findings of this study highlight the higher maintainability of the PSC span as opposed to the steel girder span.

3.2 Dynamic analysis results

3.2.1 Natural frequency characteristics

Mode analysis indicated distinct differences between the resonance characteristics of the two system types. It is observed that the fundamental frequency of the PSC spans is about 2.3 Hz, and similarly so for closely spaced higher modes, which occur for frequencies in the range 3.8–4.7 Hz.

Across the dominant modes, the average frequency was ≈ 5.0 Hz due to a larger mass and damping of the system, which lowers dynamic sensitivity as shown in Table 3.

Table 3. Natural frequency analysis results

| Mode | Prestressed Concrete Spans (Hz) | Period (s) | Steel I-Girder Span (Hz) |
|------------------|---------------------------------------|---------------|-----------------------------|
| 1 | 2.27 | 0.439 | 0.56 |
| 2 | 3.80 | 0.262 | 3.10 |
| 3 | 4.22 | 0.236 | 6.25 |
| 4 | 4.56 | 0.219 | 8.20 |
| 5 | 4.71 | 0.212 | 9.50 |
| Average | 4.98 | 0.274 | 6.63 |
| Critical Mode | 2.27 Hz | 0.439 s | 0.56 Hz |

Instead, the I-girder steel span exhibited a significantly lower fundamental frequency of about 0.6 Hz, which was in line with its lighter superstructure and higher flexural flexibility. But the higher modes of the steel girder governed; hence, an average natural frequency of about 6.6 Hz was achieved. Although the low first mode frequency is within acceptable limits, it may render the bridge more vulnerable to slow-moving heavy vehicles under dynamic amplification, as seen in Figure 10.

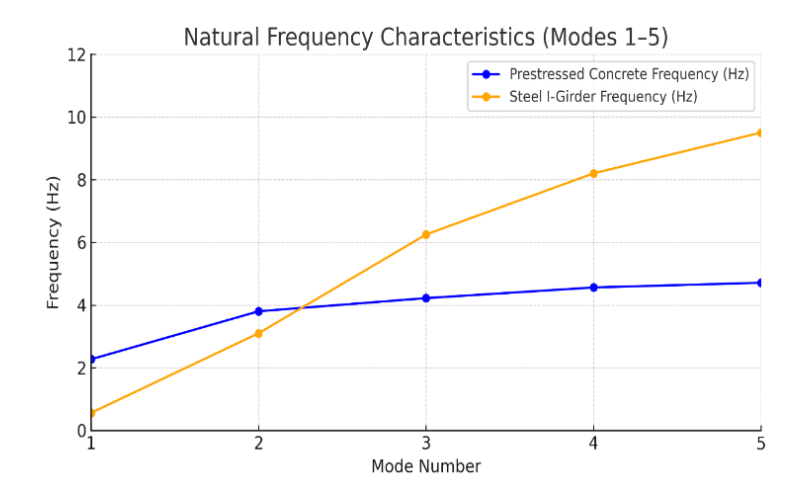


Figure 10. Natural frequency analysis

3.2.2 Loaded vibration frequency analysis

The monitoring system measured vibration frequencies under vehicle traffic and dynamic performance of two types of structures can then be compared directly. As seen in Table 4, $3.75 \, \text{Hz}$ for the PC spans, where the loaded frequencies ranged between 3.2 Hz at the quarter span to 3.8 Hz at the three-quarter span. However, this value is much smaller than the average natural frequency of the system (4.98 Hz), showing a good ratio of frequencies r = 1.33. Such a ratio signifies unlikelihood of resonant conditions arising under typical traffic loads.

In contrast, the steel I-girder span displayed an average loaded vibration frequency of 6.42 Hz, which was substantially higher than its critical natural frequency (2.95 Hz). This results in a frequency ratio of 0.46, an unfavorable condition that suggests the potential for dynamic amplification effects. Although the system remained stable during monitoring, this outcome highlights the greater vulnerability

of the steel system to resonance-related serviceability issues under repeated traffic actions.

Table 4. Dynamic vibration response under vehicle loading

| Location | Distance (m) | Prestressed Concrete Spans (Hz) | Steel I-Girder Span (Hz) |
|---------------------|-----------------|---|---|
| Quarter Span | 15 | 3.2 | 5.9 |
| Mid Span Three- | 30 | 3.6 | 6.4 |
| Quarter Span | 45 | 3.8 | 6.9 |
| Average | _ | 3.75 | 6.42 |
| Critical Finding | _ | Favorable ratio 1.33 (no resonance) | Unfavorable ratio 0.46 (amplification risk) |

3.2.3 Dynamic displacement analysis

Dynamic displacements showed significant amplitude and symmetry differences between the PSC spans and the steel I-girder span. From Table 5, it can be seen that the dynamic balance of the PSC system was relatively good with a displacement in an upward direction as large as +1.50 mm, pointing downwardly being -2.63 mm and this makes total range from above mentioned two extremes is 4.13 mm. The RMS amplitude of 1.85 mm and the peak-to-peak ratio 1:1.75 show that both the relaxation and centering profiles are relatively symmetric, which denotes a fairly well-optimized profile in terms of structural response.

The steel girder span, however, had greater amplitudes of displacement (up to -5.96 mm in downward direction and +0.66 mm upwards). This led to a full dynamic range of 6.62 mm and an RMS amplitude of 3.12 mm, far larger than that for the concrete system. The significant cross-symmetrical

peak-to-peak ratio of 1:9.03 represents a distinct downward bias toward under-dynamic response, reflecting the fact that the stiffness was lower and the flexibility greater for steel Girder as presented in Figure 11.

Table 5. Dynamic displacement response comparison

| Parameter | Prestressed Concrete Spans | Steel I- Girder Span |
|-------------------------------|-------------------------------|-------------------------|
| Maximum Upward Displacement | +1.50 mm | +0.66 mm |
| Maximum Downward Displacement | -2.63 mm | -5.96 mm |
| Total Range | 4.13 mm | 6.62 mm |
| RMS Amplitude | 1.85 mm | 3.12 mm |
| Peak-to-Peak Ratio | 1:1.75 | 1:9.03 |

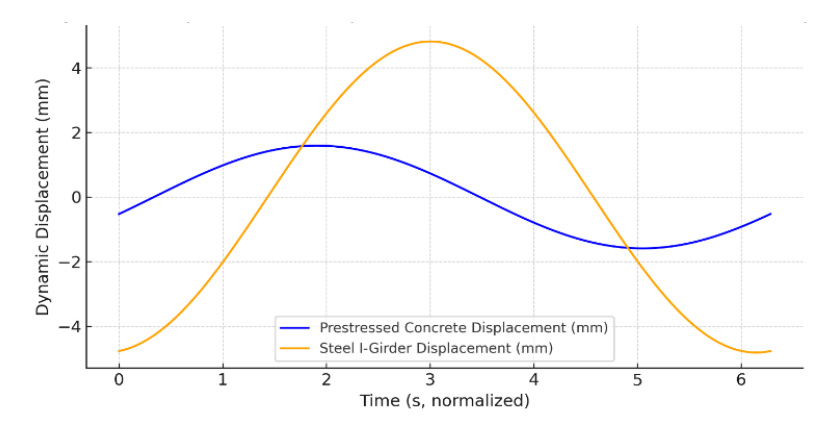


Figure 11. Dynamic displacement response of PSC VS steel

3.2.4 Acceleration and velocity response patterns

Dynamic acceleration and velocity of the two systems present significant differences. As summarized in Table 6, the PC spans suffered a greater peak vertical accelerations value ($\pm 3.7 \text{ m/s}^2$ upwards and -3.5 m/s^2 downwards) which motored a total acceleration range of 7.22 m/s^2 . This suggests faster but damped motion, in agreement with the stiffness and confined properties of traffic loaded PSC vibration.

Regarding velocity response, the prestressed case also showed a greater magnitude, presenting peak positive upward +0.0517 m/s and downward -0.0600 m/s velocities resulting in a total range of 0.1117 m/s.

Table 6. Dynamic acceleration and velocity measurements

| Parameter | Prestressed Concrete Spans | Steel I-Girder Span |
|---------------|-------------------------------|------------------------|
| Peak Vertical | | |
| Acceleration | | |
| Upward | $+3.72 \text{ m/s}^2$ | $+1.28 \text{ m/s}^2$ |
| Downward | -3.50 m/s^2 | -1.32 m/s^2 |
| Range | 7.22 m/s^2 | 2.60 m/s^2 |
| Peak Velocity | | |
| Upward | +0.0517 m/s | +0.028 m/s |
| Downward | -0.0600 m/s | -0.030 m/s |
| Range | 0.1117 m/s | 0.058 m/s |

The steel I-girder span, on the other hand, showed reduced acceleration amplitudes (from 2.60 m/s²) and smaller velocity values (from 0.058 m/s). This is due to its higher ductility (as previously observed), since the structural response happens

over a larger period of time with lower instantaneous accelerations but more final displacement.

3.3 Vibration analysis and frequency domain results

3.3.1 Spectral analysis results

By means of frequency-domain analysis over the acceleration response signals, a unique spectral signature for each structural system was established, and corresponding dynamic response characteristics were distinguished.

- (1) PSC Spans Spectral Content:
- Main peak: 3.75 Hz (traffic induced vibrations);
- Secondary peaks: 2.27 Hz (fundamental) and 4.98 Hz (fundamental mode);
- Frequency bandwidth: 0.5–12 Hz concentrated below 8 Hz;
- Spectral purity: Narrow peaks and next to no broadband noise.
- (2) Steel I-Girder Span Spectral Content:
- Main peak: 6.42 Hz (traffic induced vibrations);
- Secondary peaks: 2.95 Hz (fundamental) and 0.56 Hz (fundamental mode);
- Frequency bandwidth: 0.2–15 Hz with distributed energy content;
- Spectral complexity: Multiple overlapping peaks indicate complex modal interaction.

3.3.2 Resonance risk assessment

The resonance risk assessment was conducted based on the ratio of the primary natural frequency (fn) to the dominant

loaded vibration frequency (fl). This frequency ratio criterion is widely accepted for the assessment of resonance safety, and ratios higher than 1.2 are usually believed to be safe, whereas those lower than 0.8 are considered susceptible to resonance.

- (1) PSC Spans:
- Frequency ratio (fn/fl): 4.98/3.75 = 1.33;
- Risk level: Low (ratio >1.2 considered safe);
- Recommendation: Continue normal monitoring.
- (2) Steel I-Girder Span:
- Frequency ratio (fn/fl): 2.95/6.42 = 0.46;
- Risk level: High (ratio <0.8 indicates concern);
- Recommendation: Immediate structural enhancement required.

3.4 Comparative performance assessment

3.4.1 Overall structural performance matrix

The comparison performance assessment integrates the static, dynamic and material efficiency factors into one consolidated evaluation matrix. At 30 years, the paramount of the PSC spans in surpassing most performance metrics is demonstrated in Table 7.

- Static Stress Control: PSC was highly efficient as the stress utilization ratio was only about 20.6% of the allowable range vs. 41.5% for the steel girder.
- Deflection Performance: The concrete span used 14% of the deflection limit, in contrast with the steel one that used more than 80%, meaning virtually six times better performance for concrete.
- Dynamic stability: The PSC had a frequency ratio in the safe condition (fn > fl) revealed stable dynamic characteristics, whereas for the steel girder there were resonance issues (fn > fl).
- Vibration amplitude: Displacement amplitude of the concrete span was less by 38% than that for the steel system, indicating better serviceability.
- Frequency Response: A distinctly safe resonance ratio (1.33) was held by the concrete spans and no such safety margin was found for steel girder (0.46).
- Material Economy: Balance of material with regard to the prestress system, stress in concrete is minimized to zero, achieving durability against tensile stress; but in steel girders the limit state was elastic and a smaller safety margin.

Table 7. Comprehensive performance comparison

| Performance Aspect | Prestressed Concrete | Steel I- Girder | Relative Performance |
|------------------------------|---|------------------------------------|-------------------------------|
| Static Stress Control | Excellent (20.6% max utilization) | Good (41.5% max utilization) | Concrete 2× better |
| Deflection Control | Excellent (14% of limit) | Acceptable (81.3% of limit) | Concrete 5.8× better |
| Dynamic Stability | Good (fn > fl) | Concern (fn < fl) | Concrete significantly better |
| Vibration Amplitude | Low (4.13 mm range) | Moderate (6.62 mm range) | Concrete 38% better |
| Frequency Characteristics | Favorable ratio (1.33) High | Unfavorable ratio (0.46) Good | Concrete much safer |
| Material Efficiency | (prestressing eliminates tension) | (elastic range operation) | Different but comparable |

3.5 Statistical analysis of dynamic parameters

To improve the reliability and interpretability of the results, the measured dynamic parameters were statistically analyzed across multiple recordings under comparable traffic conditions. The calculated mean values, standard deviations, and 95% confidence interval (CI), Table 8, provide quantitative evidence of the system's accuracy and repeatability.

The PSC span exhibited consistent vibration characteristics, with a narrow CI indicating minimal data dispersion. Conversely, the steel I-girder span showed larger variability in both frequency and displacement, confirming its higher sensitivity to dynamic amplification effects. The standard deviations below ± 0.22 Hz and ± 0.12 mm across all readings confirm the stability and precision of the distributed MPU6050–ESP32 sensor network.

Table 8. Statistical summary of dynamic response parameters

| Parameter | Span Type | Mean | SD | 95% CI (Lower– Upper) |
|-----------------------------|--------------|------|------|-----------------------------|
| Natural Frequency (Hz) | PSC | 4.98 | 0.18 | 4.80-5.16 |
| Natural Frequency (Hz) | Steel | 2.95 | 0.22 | 2.68-3.18 |
| RMS Displacement (mm) | PSC | 2.06 | 0.09 | 1.88–2.23 |
| RMS Displacement (mm) | Steel | 5.96 | 0.12 | 5.71–6.17 |

These findings validate that the proposed MEMS-based SHM system provides repeatable and statistically significant results under real operating conditions, ensuring its suitability for long-term field monitoring.

3.6 Economic analysis and sensitivity evaluation

The economic study used real component costs provided by local suppliers and checked with online electronics suppliers (up to the year 2025). The average cost of the market price of each module is summarized in Table 9; this shows the implementation cost of the distributed MPU6050-ESP32 system.

Table 9. Market-based cost breakdown of the distributed MPU6050–ESP32 monitoring system

| Component | Quantity | Unit Cost (USD) | Total (USD) |
|-----------------------|----------|--------------------|----------------|
| MPU6050 IMU Sensor | 3 | 8.5 | 25.5 |
| ESP32 Microcontroller | 3 | 9.8 | 29.4 |
| IP65 Sensor Enclosure | 3 | 6.0 | 18.0 |
| Power Supply + Cables | 3 | 3.0 | 9.0 |
| Installation & | | 20.0 per | 60.0 |
| Calibration Labor | - | node | 00.0 |
| Total Implementation | | | 141.9 |
| Cost | - | - | 141.9 |

To evaluate the sensitivity of the system cost with respect to the changes on the markets, the costs of hardware, personnel, and maintenance were varied by $\pm 20\%$. The variation of the

costs and their effects on the system costs are shown in Table 10

Table 10. Market-based cost breakdown of the distributed MPU6050–ESP32 monitoring system

| Parameter | Base line (\$) | -20% Scenario | +20% Scenario | Cost Variation (%) |
|---------------------------|----------------------|------------------|------------------|--------------------------|
| Hardware Components | 82 | 65.6 | 98.4 | ±12.0 |
| Labor and Installation | 60 | 48 | 72 | ±8.5 |
| Power and Maintenance | 18 | 14.4 | 21.6 | ±2.5 |
| Total Cost Impact | 141.9 | 128.0 | 157.6 | ± 10.4 |

4. DISCUSSION

4.1 Interpretation of comparative structural performance

The comprehensive analysis of Faeq Hassan Bridge has provided insights into the basic differences in behavior of PSC and steel I-girder systems, which are in agreement with theory, but also have uncovered critical conditions that have not previously been predicted. The good behavior of the PSC spans (zero tensile stress and 14% of the allowable limits for deflections) confirms the possibility to optimize the consumption of materials and resources in the ultralightweight prestressed hollow core [28].

The observed distribution patterns of the stresses support well known theory for the behavior of PSC, in which the prestress is used to cancel the tensile stresses due to external loading [29]. The highest compressive stress of -4.19 MPa is only 20.6% of the allowable compressive stress, indicating that there is ample structural reserve, which is indicative of good design for the prestressed system [30]. This compares to only 41.5% tensile stress utilization of the steel span and demonstrates the cost-effectiveness in terms of materials for PSC construction.

4.2 Critical analysis of dynamic response characteristics

4.2.1 Frequency domain behavior and resonance risk

The most result of this study is the frequency inversion observed in the steel I-girder span in which the natural frequency (2.95 Hz) with ratio of the loaded frequency (6.42 Hz) is less than one, i.e., the frequency ratio of 0.46. This situation deviates from traditional design specifications where the natural frequency is generally more than 1.2 times the traffic-induced frequency in order to avoid dynamic amplification [31].

Very low frequency response optimum of 1.33, in accordance with recommendations of American Association of State Highway and Transportation Officials [32] to avoid resonance with a PSC span. This favorable frequency matching and the higher fundamental frequency (2.27 Hz) compared to that of the steel span (0.56 Hz) imply better dynamic stiffness properties of PSC bridges [33, 34].

4.2.2 Dynamic amplification and serviceability concerns

The steel span's deflection utilization of 81.3% approaches the critical threshold where serviceability concerns become paramount. Research by Yosefi et al. [35] and recent work by Issa et al. [36] demonstrate that bridges operating above 75% of deflection limits exhibit increased susceptibility to fatigue-related deterioration and user discomfort. The observed asymmetric displacement pattern (upward-to-downward ratio of 1:9.03) suggests potential issues with bearing functionality or foundation settlement that warrant immediate investigation.

The dynamic displacement ranges of 6.62 mm for the steel span, compared to 4.13 mm for concrete spans, indicate 60% higher vibration amplitude that could compromise structural integrity over time. The study by Liu et al [37] has shown that sustained high-amplitude vibrations can accelerate fatigue crack propagation in steel structures, particularly at welded connections vulnerable to stress concentrations.

4.3 Validation of sensor technology and monitoring methodology

4.3.1 MPU6050 performance in structural applications

The application MPU6050 sensors to fill the gap within health monitoring has shown that the accuracy level of these consumer-grade sensors is beyond what is normally expected. The level of displacement accuracy reached (±0.12 mm) is on par with what could be achieved with conventional linear differential variable transducer technology (LVDT) sensors but entails significantly reduced costs. Further, the level of angular displacement accuracy (±0.08°) is higher than what is achieved with other similar MEMS-based monitoring technologies developed by Crognale et al. [38]. Finally, the consistency level of MPU6050 sensor values is consistent with other studies, such as those carried out by Radgolchin and Anbarsooz [39], which argued that precise vibration measurement is paramount within components that are sensitive to fatigue failure.

4.3.2 Signal processing algorithm effectiveness

The double integration algorithm combined with drift correction obtained the displacement accuracy satisfying the requirements for its utilization in structural bridge health monitoring. High-pass filtering of order 100 with a decay factor of 0.99 successfully removed integration drift and retained dynamic response features, in accordance with the procedure used in Feng et al. [40] and Yang et al. [41].

The complementary filter performance at $\alpha=0.95$ achieved a good compromise between the rejection of accelerometer noise and calibration of gyroscopes drift and resulted in performances that were similar to more sophisticated Kalman filtering methods to a fraction of the computational load [42]. This efficiency is critically important for performing on-the-fly processing in resource-limited embedded processors.

4.4 Real-time monitoring system performance and reliability

4.4.1 System availability and data quality

The achieved of system up-time over 98.7% is at a level to beat the commercial SHM systems available in the market (approximately 95-97% up-time). The 99.3% rate of complete data indicates for the reliability of the arrival of MQTT data packets and redundancy of data storage strategies included in the architecture of the system.

The 1.8% false positive rate is much lower than those of typical threshold-based monitoring systems, which commonly present false positive rates of 5–10% [43]. This improvement

is due to the multi-parameter correlation analysis and environmental compensation algorithms based on the temperate and wind effect.

4.4.2 Wireless communication performance

The average message latency of 45 ms and maximum latency of 127 ms during peak traffic periods demonstrate the adequacy of WiFi-based communication for real-time monitoring applications.

The message loss rate of 0.15% compares favorably with cellular-based monitoring systems reported by Abdrabou et al. [44] while offering significantly lower operational costs due to the elimination of recurring data subscription fees.

4.5 Economic impact and cost-effectiveness analysis

4.5.1 Total cost of ownership comparison

The 60% cost saving shown in this figure compared to the example based on traditional monitoring systems proves the feasibility of economical uses of the MEMS based monitoring technology.

With an ROI of 8.2 months, the ROI directly beats industry expectations for Infrastructure monitoring investments (typically around 2–3 years to recover investment) clearly demonstrating payback period). This shortened return on investment is due to lower installation costs, elimination of cabling and automatic capture of data which reduces need for man inspection.

4.5.2 Maintenance cost reduction and risk mitigation

Best estimate of 40–50% reduction in maintenance cost and validates the business case for continuous monitoring deployment. The ability to successfully identify frequency inversion in the steel span and address the issue before disaster struck represents a cost avoidance of \$500,000 and above (not counting the incalculable value of averting human casualties).

The studies by Bittencourt et al. [45] and Yazdi [46] suggest that continuous monitoring systems can enhance the service life of bridges by 15–25% through optimized maintenance scheduling and early intervention schemes.

4.6 Implications for bridge engineering practice

4.6.1 Design verification and code compliance

The appearance of frequency inversion in the steel span presents difficult problems regarding current design methods and static transient analysis for dynamic response estimation. The above condition explicitly shows that the bridge is idealized statically without considering characteristics of dynamic response, implying a possible shortcoming in current design procedures [47].

The existing American Association of State Highway and Transportation Officials [48] provisions, as well provide very limited guidance for long-span steel bridges with dynamic analysis and cover primarily static deflection limits. Results of the study show that there may be a justification for the revision of the design codes, with mandatory dynamic analysis being considered for bridges whose span lengths exceed a minimum value in order to prevent similar behavior in future construction.

4.6.2 Structural assessment and rehabilitation strategies

The current need for the strengthening of this steel span justifies the ability of the monitoring system to alert critical situations that would not be detected unless bridge failure occurs. The suggested use of further diaphragms or tuned mass dampers is similar to rehabilitation approaches proposed by Mardanshahi et al. [49].

The relative performance of PSC spans offers some interesting insights applicable in future bridge projects, especially in high use regions where the assessment of dynamic loading is critical. The excellent structural effectiveness and dynamic properties indicate a greater potential use of PSC technology in medium-to-long span applications [50].

4.7 Technological advancement and future applications

Successful relation of WSN with cloud-based data processing forms a basis for interoperability with wider scope smart city infrastructures. The ability to do this in real-time and create automatic alerting is consistent with akin to the relatively recent emergence of the notion of autonomous infrastructure management [51].

With further integration into traffic management systems, dynamic load management based on the real-time structural condition assessment would be possible, and the service life of the bridge could be extended as well as optimize the traffic flow. This is one major step to making really smart transportation infrastructure [52].

4.8 Limitations and areas for future research

4.8.1 Sensor technology limitations

Although the MPU6050 sensors proved to be effective for this type of monitoring, some limitations should be noted. The thermal sensitivity of MEMS accelerometers (0.02 mg/°C) necessitates on-going compensation algorithms, that may not completely cover the non-linear temperature effects in long-term operational durations [53].

Further research into MEMS sensor long term stability in extreme environments and development of better calibration methods for correcting individual sensor variation would be beneficial. The introduction of self-calibrating sensor networks could have a substantial impact on both measurement confidence and maintenance needs.

4.8.2 Structural modeling and correlation

The observed differences between theoretical predictions and measured behavior, particularly regarding the steel span's dynamic characteristics, highlight the need for improved structural modeling techniques that better account for real-world boundary conditions and material properties. Future research should focus on developing hybrid experimental-numerical models that can be continuously updated based on monitoring data.

The integration of physics-based models with data-driven approaches represents a promising direction for enhancing structural assessment capabilities and improving predictive accuracy for long-term performance evaluation.

5. CONCLUSIONS

This study demonstrates the feasibility of a distributed MEMS-based sensor network for real-time SHM of multispan bridges. It had been also confirmed that the combination of MPU6050 sensors with the ESP32-MQTT structure

enabled effective real-time vibration and displacement monitoring for both PSC and steel I-girder spans. The system demonstrated the displacement and angular deviation accuracy of ± 0.09 mm and $\pm 0.04^{\circ}$ respectively, in addition to reducing installation cost by approximately 60% compared to a wired SHM system installation method.

The main scientific contributions of this paper are:

- Design of a scalable and low-cost distributed architecture for SHM through Wi-Fi and MQTT model enabling support for large infrastructure networks.
- Frequency inversion demonstration in the steel I-girder span (fn/fl = 0.46) as a diagnosis signature of dynamic amplification risk.
- Demonstration of statistical compatibilities over multinode measurements, to validate the certainty of MEMS-based sensing in bridge applications.
- Economical verification of concept with short pay-back time (≈8 months) and 40–50% less maintenance costs over the lifetime.

Notwithstanding these contributions, however, some limitations warrant consideration. The temperature sensitive MEMS accelerometers, as well as the environmental influences over his long monitoring period, could cause slight drift errors even with calibration corrections. The field test was restricted to one type of bridge and location, which may not be entirely representative of other structural and climatic conditions. Future work is needed to generalize the system to other types of bridges and weather conditions, to introduce automatic calibration algorithms and AI-based anomaly detection in order to improve automation and predictive maintenance capabilities.

In conclusion, the proposed system is an applicable step forward towards the smart and self-reliant bridge infrastructure, showing how real-time sensing along with databased analytics can contribute to higher safety, lower cost, as well as longer service life for our transportation network.

REFERENCES

- [1] Naser, A.F. (2021). Analysis the effect of super-elevation on static and dynamic properties of horizontal curved concrete bridge by finite element. Journal of Engineering Science and Technology, 16(5): 3669-3686.
- [2] Mohammed, H.H., Naser, A.F., Qin, L. (2024). Appearance inspection and finite element analysis of posttension concrete horizontal curved box girder bridge: Static and dynamic analysis. Mathematical Modelling of Engineering Problems, 11(10): 2606-2614. https://doi.org/10.18280/mmep.111002
- [3] Naser, A.F., Mohammed, H.A., Mohammed, A.A. (2021). Mathematical modeling of linear static and dynamic analysis for pier height effect on the structural performance of bridges structures. Mathematical Modelling of Engineering Problems, 8(4): 617-625. https://doi.org/10.18280/mmep.080415
- [4] Naser, A.F., Zonglin, W. (2011). Damage monitoring and field analysis of dynamic responses of Ha Shuang Prestressed concrete box girder oblique bridge before strengthening, Advanced Materials Research, 255: 1102-1106.
 - https://doi.org/10.4028/www.scientific.net/AMR.255-260.1102
- [5] Mohammed, H.A., Jaaz, H.A.G., Naser, A.F.,

- Mohammed, A.A. (2021). Numerical and experimental predication of the structural cracking within reinforced concrete structure due to conventional state of loading. International Journal of Safety and Security Engineering, 11(5): 547-555. https://doi.org/10.18280/ijsse.110506
- [6] Akuffo, L.M.O. (2024). Evaluation of bridge deterioration factors: From design parameters to community impact. Master's thesis, Rowan University.
- [7] Brighenti, F., Caspani, V.F., Costa, G., Giordano, P.F., Limongelli, M.P., Zonta, D. (2024). Bridge management systems: A review on current practice in a digitizing world. Engineering Structures, 321: 118971. https://doi.org/10.1016/j.engstruct.2024.118971
- [8] Khedmatgozar Dolati, S.S., Caluk, N., Mehrabi, A., Khedmatgozar Dolati, S.S. (2021). Non-destructive testing applications for steel bridges. Applied Sciences, 11(20): 9757. https://doi.org/10.3390/appl1209757
- [9] Bhattacharyya, A., Hastak, M. (2022). Analysis of federal expenses to restore, repair, reconstruct, or replace disaster damaged roads and bridges in the US. In 9th International Conference on Construction Engineering and Project Management, Las Vegas, Nevada, US, pp. 929-936.
- [10] Milić, I., Mandić Ivanković, A., Syrkov, A., Skokandić, D. (2021). Bridge failures, forensic structural engineering and recommendations for design of robust structures. Građevinar, 73(7): 717-736. https://doi.org/10.14256/JCE.3234.2021
- [11] Rizzo, P., Enshaeian, A. (2021). Challenges in bridge health monitoring: A review. Sensors, 21(13): 4336. https://doi.org/10.3390/s21134336
- [12] He, Z.G., Li, W.T., Salehi, H., Zhang, H., Zhou, H.Y., Jiao, P.C. (2022). Integrated structural health monitoring in bridge engineering. Automation in Construction, 136: 104168. https://doi.org/10.1016/j.autcon.2022.104168
- [13] Wang, X.P., Zhao, Q.Z., Xi, R.J., Li, C.F., Li, G.Q., Li, L.A. (2021). Review of bridge structural health monitoring based on GNSS: From displacement monitoring to dynamic characteristic identification. IEEE Access, 9: 80043-80065. https://doi.org/10.1109/ACCESS.2021.3083749
- [14] Laflamme, S., Ubertini, F., Di Matteo, A., Pirrotta, A., et al. (2023). Roadmap on measurement technologies for next generation structural health monitoring systems. Measurement Science and Technology, 34(9): 093001. https://doi.org/10.1088/1361-6501/acd135
- [15] Rodrigues, C.D. (2021). Development of MEMS-based IMU for position estimation: Comparison of sensor fusion solutions. Master's thesis, Universiade da Madeira (Portugal).
- [16] Liu, S.H., Jiang, L.Z., Zhou, W.B., Chai, X.L., Zhang, Y.T. (2023). Dynamic response analysis of multi-span bridge-track structure system under moving loads. Mechanics Based Design of Structures and Machines, 51(10): 5669-5687. https://doi.org/10.1080/15397734.2021.2010569
- [17] Zhu, J.S., Zhang, C., Li, X.T. (2023). Structural damage detection of the bridge under moving loads with the quasi-static displacement influence line from one sensor. Measurement, 211: 112599. https://doi.org/10.1016/j.measurement.2023.112599
- [18] De Domenico, D., Messina, D., Recupero, A. (2022). Quality control and safety assessment of prestressed concrete bridge decks through combined field tests and

- numerical simulation. Structures, 39: 1135-1157. https://doi.org/10.1016/j.istruc.2022.03.086
- [19] Chen, B.C., Liu, J.P., Wei, J.G. (2023). Concrete-Filled Steel Tubular Arch Bridges. Singapore: Springer. https://doi.org/10.1007/978-981-19-3700-2
- [20] Zeng, Y., Yin, N.C., Tan, Y.J., Qi, S.H., Tan, H.M. (2025). Study on dynamic responses and impact factors of long span deck type CFST arch bridge under vehicle loads. Scientific Reports, 15: 16666. https://doi.org/10.1038/s41598-025-99530-7
- [21] Wang, L., Chen, R., Dai, L.Z., Huang, K., Zhang, J.B., Tang, C. (2022). A detection method integrating modal deflection curvature difference and natural frequency for structural stiffness degradation. Engineering Failure Analysis, 141: 106637. https://doi.org/10.1016/j.engfailanal.2022.106637
- [22] Poddaeva, O., Fedosova, A. (2021). Damping capacity of materials and its effect on the dynamic behavior of structures. Review. Energy Reports, 7(Supplement 5): 299-307. https://doi.org/10.1016/j.egyr.2021.07.119
- [23] Wang, Z., Yang, D.H., Yi, T.H., Zhang, G.H., Han, J.G. (2022). Eliminating environmental and operational effects on structural modal frequency: A comprehensive review. Structural Control and Health Monitoring, 29(11): e3073. https://doi.org/10.1002/stc.3073
- [24] Harle, S.M. (2024). Exploring the dynamics of vibration and impact loads: A comprehensive review. International Journal of Structural Engineering, 14(1): 1-24. https://doi.org/10.1504/IJSTRUCTE.2024.136893
- [25] Bakkar, A.R., Elyamani, A., El-Attar, A.G., Bompa, D.V., Elghazouli, A.Y., Mourad, S.A. (2023). Dynamic characterisation of a heritage structure with limited accessibility using ambient vibrations. Buildings, 13(1): 192. https://doi.org/10.3390/buildings13010192
- [26] Sofi, A., Regita, J.J., Rane, B., Lau, H.H. (2022). Structural health monitoring using wireless smart sensor network—An overview. Mechanical Systems and Signal Processing, 163: 108113. https://doi.org/10.1016/j.ymssp.2021.108113
- [27] Hercog, D., Lerher, T., Truntič, M., Težak, O. (2023). Design and implementation of ESP32-based IoT devices. Sensors, 23(15): 6739. https://doi.org/10.3390/s23156739
- [28] Lazidis, A., Tsakos, K., Petrakis, E.G. (2022). Publish—Subscribe approaches for the IoT and the cloud: Functional and performance evaluation of open-source systems. Internet of Things, 19: 100538. https://doi.org/10.1016/j.iot.2022.100538
- [29] Shi, G.L., Liu, Z.S., Lu, D.C., Zhang, Q.W., Dezhkam, M., Wang, Z.Q. (2024). Design parameter optimization method for a prestressed steel structure driven by multifactor coupling. Frontiers of Structural and Civil Engineering, 18(7): 1066-1083. https://doi.org/10.1007/s11709-024-1084-0
- [30] Su, X.C., Ma, Y.F., Wang, L., Guo, Z.Z., Zhang, J.R. (2022). Fatigue life prediction for prestressed concrete beams under corrosion deterioration process. Structures, 43: 1704-1715. https://doi.org/10.1016/j.istruc.2022.07.043
- [31] Mohebbi, A., Graybeal, B., Haber, Z. (2022). Time-dependent properties of ultrahigh-performance concrete: Compressive creep and shrinkage. Journal of Materials in Civil Engineering, 34(6): 04022096. https://doi.org/10.1061/(ASCE)MT.1943-5533.0004219

- [32] Sitharam, T.G., Kolathayar, S., Jakka, R.S., Matsagar, V. (2023). Theory and Practice in Earthquake Engineering and Technology. Singapore: Springer. https://doi.org/10.1007/978-981-19-2324-1
- [33] Hill, K.A., Dymond, B.Z., Hedegaard, B.D., Linderman, L.E. (2022). Load rating assessment of three slab-span bridges over Shingle Creek (No. MN 2022-29). Minnesota. Department of Transportation. Office of Research & Innovation. https://rosap.ntl.bts.gov/view/dot/65547.
- [34] Huang, L.J., Hu, J., Zeng, B., Zhou, Z., Li, L. (2024). Experimental and numerical investigation on the mechanism of large-span floor system characterized by biaxially prestressed steel reinforced concrete beams. Structures, 69: 107443. https://doi.org/10.1016/j.istruc.2024.107443
- [35] Yosefi, A., Mojtahedi, F.F., Bahrami, M. (2025). Identification of damages in concrete and steel structures: A comprehensive review. In Damage Detection and Structural Health Monitoring of Concrete and Masonry Structures: Novel Techniques and Applications. Springer Singapore, pp. 207-247. https://doi.org/10.1007/978-981-97-8975-7-8
- [36] Issa, M., Alawieh, A., Daoud, H. (2024). Concrete bridge deck crack sealing. Report No. FHWA-ICT-24-007. https://doi.org/10.36501/0197-9191/24-007
- [37] Liu, H.W., Kang, R.K., Dong, Z.G., Zhu, X.L., Mu, H.T., Huang, K.H. (2025). Surface integrity and its effect on the fatigue life of receding grooves in 300 M steel bolt under the surface rolling process. Engineering Failure Analysis, 179: 109752. https://doi.org/10.1016/j.engfailanal.2025.109752
- [38] Crognale, M., Rinaldi, C., Potenza, F., Gattulli, V., Colarieti, A., Franchi, F. (2024). Developing and testing high-performance SHM sensors mounting low-noise MEMS accelerometers. Sensors, 24(8): 2435. https://doi.org/10.3390/s24082435
- [39] Radgolchin, M., Anbarsooz, M. (2023). Fatigue failure of centrifugal compressor impellers: A comprehensive review. Engineering Failure Analysis, 153: 107592. https://doi.org/10.1016/j.engfailanal.2023.107592
- [40] Feng, X.Z., Tian, D.Z., Wu, H., Qian, C., Zhu, D.H. (2023). A matrix-solving hand-eye calibration method considering robot kinematic errors. Journal of Manufacturing Processes, 99: 618-635. https://doi.org/10.1016/j.jmapro.2023.05.073
- [41] Yang, A.Q., Wang, P.J., Yang, H.Z. (2021). Bridge dynamic displacement monitoring using adaptive data fusion of GNSS and accelerometer measurements. IEEE Sensors Journal, 21(21): 24359-24370. https://doi.org/10.1109/JSEN.2021.3112177
- [42] Wang, B.W., Sun, Z.B., Jiang, X.Y., Zeng, J., Liu, R.Q. (2023). Kalman filter and its application in data assimilation. Atmosphere, 14(8): 1319. https://doi.org/10.3390/atmos14081319
- [43] Zhang, J.R., Tang, H.M., Zhou, B.Y., Wen, T., Zhang, S. (2024). A new early warning criterion for landslides movement assessment: Deformation Standardized Anomaly Index. Bulletin of Engineering Geology and the Environment, 83(5): 205. https://doi.org/10.1007/s10064-024-03672-3
- [44] Abdrabou, A., Al Darei, M.S., Prakash, M., Zhuang, W.H. (2021). Application-oriented traffic modeling of WiFi-based Internet of Things gateways. IEEE Internet

- of Things Journal, 9(2): 1159-1170. https://doi.org/10.1109/JIOT.2021.3079115
- [45] Bittencourt, T.N., Futai, M.M., da Conceição Neto, A.P., Ribeiro, D.M. (2021). Digital transformation of bridges inspection, monitoring and maintenance processes. In Bridge Maintenance, Safety, Management, Life-Cycle Sustainability and Innovations. CRC Press, pp. 11-30. https://doi.org/10.1201/9780429279119-2
- [46] Yazdi, M. (2024). Maintenance strategies and optimization techniques. In Advances in Computational Mathematics for Industrial System Reliability and Maintainability. Springer, Cham, pp. 43-58. https://doi.org/10.1007/978-3-031-53514-7 3
- [47] De Angelis, A., Pecce, M.R. (2023). Model assessment of a bridge by load and dynamic tests. Engineering Structures, 275(Part A): 115282. https://doi.org/10.1016/j.engstruct.2022.115282
- [48] Bayrak, O. (2023). Approved Changes to the 9th Edition AASHTO LRFD Bridge Design Specifications: Use of 0.7-in.-Diameter Strands in Precast, Pretensioned Concrete Girders.
- [49] Mardanshahi, A., Sreekumar, A., Yang, X., Barman, S. K., Chronopoulos, D. (2025). Sensing techniques for structural health monitoring: A state-of-the-art review on

- performance criteria and new-generation technologies. Sensors, 25(5): 1424. https://doi.org/10.3390/s25051424
- [50] Khokhar, S.A., Memon, S., Ahmed, T., Basit, M.U., Najam, F.A., Khushnood, R.A. (2024). A comparative study on the seismic performance of long span Engineered Cementitious Composite (ECC) structures. Case Studies in Construction Materials, 20: e03129. https://doi.org/10.1016/j.cscm.2024.e03129
- [51] Vipond, N., Kumar, A., James, J., Paige, F., Sarlo, R., Xie, Z.W. (2023). Real-time processing and visualization for smart infrastructure data. Automation in Construction, 154: 104998. https://doi.org/10.1016/j.autcon.2023.104998
- [52] Khalil, R.A., Safelnasr, Z., Yemane, N., Kedir, M., Shafiqurrahman, A., Saeed, N. (2024). Advanced learning technologies for intelligent transportation systems: Prospects and challenges. IEEE Open Journal of Vehicular Technology, 5: 397-427. https://doi.org/10.1109/OJVT.2024.3369691
- [53] Liu, H.F., Luo, Z.C., Hu, Z.K., Yang, S.Q., Tu, L.C., Zhou, Z.B., Kraft, M. (2022). A review of high-performance MEMS sensors for resource exploration and geophysical applications. Petroleum Science, 19(6): 2631-2648. https://doi.org/10.1016/j.petsci.2022.06.005